Laser-induced transient magnons in $Sr_3Ir_2O_7$ throughout the Brillouin zone

Daniel G. Mazzone[a,b,1], Derek Meyers[a,c,1], Yue Cao[a,d], James G. Vale[e], Cameron D. Dashwood[e], Youguo Shi[f], Andrew J. A. James[g], Neil J. Robinson[h], Jiaqi Lin[a,i], Vivek Thampy[j], Yoshikazu Tanaka[k], Allan S. Johnson[l], Hu Miao[a], Ruitang Wang[i], Tadesse A. Assefa[a,2], Jungho Kim[m], Diego Casa[m], Roman Mankowsky[n], Diling Zhu[o], Roberto Alonso-Mori[o], Sanghoon Song[o], Hasan Yavas[o], Tetsuo Katayama[k], Makina Yabashi[k], Yuya Kubota[k], Shigeki Owada[k], Jian Liu[p], Junji Yang[p], Robert M. Konik[a], Ian K. Robinson[a,e], John P. Hill[q], Desmond F. McMorrow[e], Michael Först[n], Simon Wall[l,r,3], Xuerong Liu[i,3], and Mark P. M. Dean[a,3]

[a]Condensed Matter Physics and Materials Science Department, Brookhaven National Laboratory, Upton, NY 11973; [b]Laboratory for Neutron Scattering and Imaging, Paul Scherrer Institut, CH-5232 Villigen, Switzerland; [c]Department of Physics, Oklahoma State University, Stillwater, OK 74078; [d]Materials Science Division, Argonne National Laboratory, Argonne, IL 60439; [e]London Centre for Nanotechnology and Department of Physics and Astronomy, University College London, London WC1E 6BT, United Kingdom; [f]Beijing National Laboratory for Condensed Matter Physics, Institute of Physics, Chinese Academy of Sciences, Beijing 100190, China; [g]School of Physical Sciences, The Open University, Milton Keynes MK7 6AA, United Kingdom; [h]Institute for Theoretical Physics, University of Amsterdam, 1098 XH Amsterdam, The Netherlands; [i]School of Physical Science and Technology, ShanghaiTech University, Shanghai 201210, China; [j]Stanford Synchrotron Radiation Lightsource, SLAC National Accelerator Laboratory, Menlo Park, CA 94025; [k]RIKEN SPring-8 Center, Sayo 679-5148, Japan; [l]ICFO – The Institute of Photonics Sciences, The Barcelona Institute of Science and Technology, 08860, Castelldefels, Barcelona, Spain; [m]Advanced Photon Source, Argonne National Laboratory, Argonne, IL 60439; [n]Max Planck Institute for the Structure and Dynamics of Matter, D-22761 Hamburg, Germany; [o]Linac Coherent Light Source, SLAC National Accelerator Laboratory, Menlo Park, CA 94025; [p]Department of Physics and Astronomy, University of Tennessee, Knoxville, TN 37996; [q]National Synchrotron Light Source II, Brookhaven National Laboratory, Upton, NY 11973; and [r]Department of Physics and Astronomy, Aarhus University, 8000 Aarhus C, Denmark

Edited by Anne L'Huillier, Lund University, Lund, Sweden, and approved April 23, 2021 (received for review February 23, 2021)

Although ultrafast manipulation of magnetism holds great promise for new physical phenomena and applications, targeting specific states is held back by our limited understanding of how magnetic correlations evolve on ultrafast timescales. Using ultrafast resonant inelastic X-ray scattering we demonstrate that femtosecond laser pulses can excite transient magnons at large wavevectors in gapped antiferromagnets and that they persist for several picoseconds, which is opposite to what is observed in nearly gapless magnets. Our work suggests that materials with isotropic magnetic interactions are preferred to achieve rapid manipulation of magnetism.

time-resolved resonant X-ray scattering | transient magnetic excitations | iridates

Ultrashort laser pulses are a powerful emerging tool to modify materials as they can induce new nonequilibrium states of matter (1–10). Particularly interesting is photoexcited magnetism, as in equilibrium magnetic fluctuations are central to many phenomena including unconventional superconductivity, charge-stripe correlations, and quantum spin liquids (11–13). While increasing experimental evidence has shown that magnetism is suppressed by photodoping, the exact nature of the spin configuration in the transient state and its evolution in time is largely unclear, holding back progress in our understanding. This is mainly because experimental tools for microscopically probing ultrafast magnetism are still in their infancy with respect to probing equilibrium magnetism. Most techniques are only sensitive to the magnetic order parameter or exclusively probe magnetic correlations at the Brillouin zone center. While often insightful, these probes cannot distinguish between various microscopic states, as their differences appear in the spacial (or Q) dependence of the magnetic correlations (see Fig. 1*A*). This is important, for instance, in studies that focus on the transient behavior of local exchange couplings, as they can be probed directly through magnons at the magnetic zone boundary. In fact, several theories predict that the magnetic exchange couplings among ordered ions change transiently under photoexcitation (14–17). Thus, clarifying which magnons are excited in the transient state and how they evolve in time is crucial to unveil the detailed nature of transient states.

We use time-resolved resonant X-ray scattering to overcome the aforementioned limitation, enabling studies of transient magnetic correlations throughout the Brillouin zone at ultrafast timescales. The technique uses incident X-rays that carry an appreciable momentum and whose energy is tuned to a core-hole resonance, enhancing the sensitivity to magnetic modes. Magnetic long-range order is measured via time-resolved resonant elastic X-ray scattering (tr-REXS). In contrast, time-resolved resonant inelastic X-ray scattering (tr-RIXS) measures the energy loss and momentum change of scattered photons, enabling probing short-range magnetic fluctuations, such as magnons, in the transient state. tr-RIXS measurements of magnons are extremely challenging technically. The first

Significance

Ultrafast manipulation of magnetic states holds great promise for progress in our understanding of new quantum states and technical applications, but our current knowledge of transient magnetism is very limited. Our work elucidates the nature of transient magnetism in gapped antiferromagnets using $Sr_3Ir_2O_7$ as a model material. We find that transient magnetic fluctuations are trapped throughout the entire Brillouin zone while remaining present beyond the time that is required to restore the original spin network. The results are interpreted in the context of a spin-bottleneck effect, in which the existence of an explicit magnetic decay channel allows for an efficient thermalization of transient spin waves.

Author contributions: D.G.M., D.M., S.W., X.L., and M.P.M.D. designed research; D.G.M., D.M., Y.C., J.G.V., C.D.D., J. Lin, V.T., Y.T., A.S.J., H.M., R.W., T.A.A., J.K., D.C., R.M., D.Z., R.A.-M., S.S., H.Y., T.K., M.Y., Y.K., S.O., J. Liu, J.Y., I.K.R., J.P.H., D.F.M., M.F., S.W., X.L., and M.P.M.D. performed research; Y.S. contributed new reagents/analytic tools; D.G.M., D.M., A.J.A.J., N.J.R., R.M.K., D.F.M., S.W., X.L., and M.P.M.D. analyzed data; and D.G.M., D.M., S.W., X.L., and M.P.M.D. wrote the paper.

The authors declare no competing interest.

This article is a PNAS Direct Submission.

[1]D.G.M. and D.M. contributed equally to this work.

[2]Present address: Stanford Institute for Materials and Energy Sciences, SLAC National Accelerator Laboratory, Menlo Park, CA 94025.

[3]To whom correspondence may be addressed. Email: liuxr@shanghaitech.edu.cn, simon.wall@phys.au.dk, or mdean@bnl.gov.

This article contains supporting information online at https://www.pnas.org/lookup/suppl/doi:10.1073/pnas.2103696118/-/DCSupplemental.

Published May 26, 2021.

PHYSICS

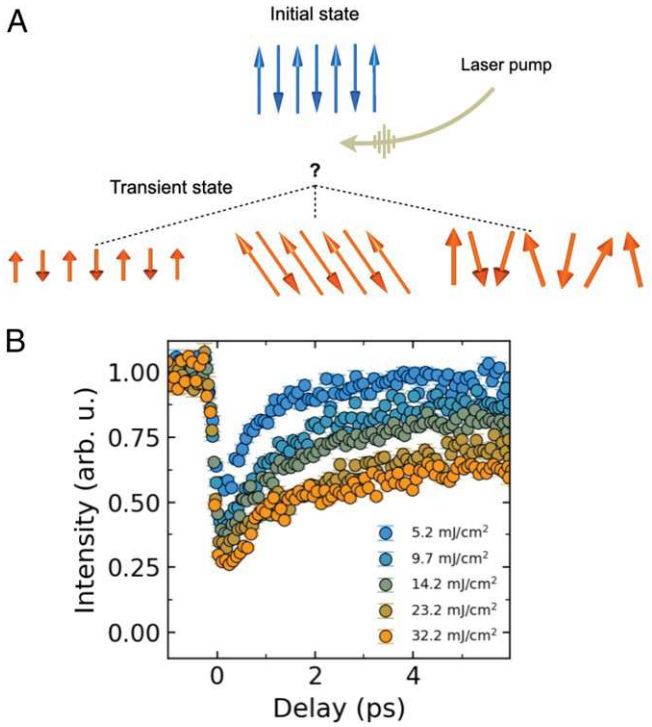

Fig. 1. Demagnetization pathways in antiferromagnets. (*A*) Multiple spin configurations can give rise to the same macroscopic magnetization. These are indistinguishable in order parameter measurements, as commonly probed in ultrafast studies. Three such cases are sketched, corresponding to a reduced magnetic moment, a collective spin rotation, and a disordered state. The first two cases are uniform perturbations to the entire spin network, whereas the latter is due to short-range disorder of individual spins. (*B*) Relative magnetic (−3.5, 1.5, 18) Bragg peak intensity in $Sr_3Ir_2O_7$ as a function of time delay (notation in reciprocal lattice units [r.l.u]). The data are plotted up to 7 ps after the arrival of the optical pump at $t = 0$. The error bars follow Poissonian statistics.

experiment was performed a few years previously on Sr_2IrO_4, but the only observable effects occurred at the magnetic ordering wavevector (2). This appears superficially congruent with the idea that the effectively zero momentum light can only excite individual magnons at the center of the magnetic Brillouin zone. Here we study gapped antiferromagnet $Sr_3Ir_2O_7$ and directly show that photoexcitation can modify magnons throughout the Brillouin zone which persist beyond a picosecond timescale. We suggest that the large spin gap in $Sr_3Ir_2O_7$ blocks the cooling of transient magnons that appears to occur in Sr_2IrO_4.

Demagnetization Pathways in Antiferromagnets

Fig. 1*B* shows the time evolution of the $Sr_3Ir_2O_7$ magnetic Bragg peak intensity up to 7 ps after the arrival of the 2-μm (620-meV) laser pump that excites carriers across the band gap (18). This was measured using Ir L_3-ege tr-REXS at $T \approx 110$ K $\ll T_N = 285$ K using the (−3.5, 1.5, 18) magnetic Bragg peak (*Materials and Methods*). Immediately after the pump, magnetism is reduced by 50 to 75% for laser fluences between 5.2 and 32.2 mJ/cm^2. This occurs faster than our time resolution of 0.15 ps, which is substantially quicker than in other materials including Sr_2IrO_4 (19). It is noted that even for strong fluences some remnant magnetic fraction is observed immediately after the laser pump, suggesting some experimental mismatch between pumped laser and probed X-ray volumes (c.f. *SI Appendix*). However, the transient signal shows signs of saturation, suggesting the pumped volume is completely demagnetized. We refer to further details on the recovery of the magnetic long-range order in *SI Appendix*. The tr-REXS results in Fig. 1*B* clearly show that a 2-μm laser pump results in an appreciable quenching of magnetic long-range order that survives on a picosecond timescale. However, the experiment does not reveal the microscopic spin configuration of the transient state. As illustrated in Fig. 1*A*, a transiently suppressed magnetic order parameter can arise from several very different microscopic configurations that give the same REXS response. We thus studied the RIXS response of the transient state to gain insight into the Q dependence of the magnetic correlations.

Transient Evolution of Magnetic Short-Range Correlations

Fig. 2 *A* and *B* display energy-loss spectra of $Sr_3Ir_2O_7$ measured at (π, π) and $(\pi, 0)$, corresponding to the magnetic Brillouin zone center and zone boundary. The blue data points correspond to RIXS spectra in the equilibrium state, showing four features: an elastic line, a collective magnon, a magnon continuum, and an orbital excitation (20–23). The collective magnon features a moderate dispersion, shifting in energy from 100 meV at (π, π) to 150 meV at $(\pi, 0)$, while the magnon continuum (250 meV) and orbital excitation (680 meV) reveal negligible dispersion. It is believed that the magnetic excitations in equilibrium arise predominantly from the combination of Heisenberg-like interactions within the iridium layers and an anisotropic exchange perpendicular to the tetragonal plane (see also *SI Appendix*) (20, 24, 25). The orbital excitation, on the other hand, can be understood considering the electronic configuration of $Sr_3Ir_2O_7$. It is defined by the five iridium valence electrons, residing in a crystal-field-derived t_{2g} orbital manifold. The ground state is further split by strong spin–orbit coupling and moderate Coulomb interactions, establishing a filled $J_{\text{eff}} = 3/2$ and half-filled $J_{\text{eff}} = 1/2$ Mott state (20, 24–26). Thus, the excitation epitomizes a transition between these two manifolds (20, 22, 23).

We have overplotted the energy-loss spectra in equilibrium (blue) with transient state data (orange). These have been prepared with a 20 mJ/cm^2 laser pulse, for which a substantial suppression of magnetic order has been found (see Fig. 2*B*). Because small drifts in the X-ray source position can result in shifts of the measured RIXS spectrum, static and pumped spectra were measured with alternate shots of the free electron laser for each delay. The time resolution of the setup equaled ∼400 fs (see *Materials and Methods* for details). At both reciprocal lattice positions we observe significant changes in the electronic correlations at $t > 0$. This is seen most clearly in the difference spectra shown in Fig. 2 *C* and *D*, evincing that the magnon and orbital excitations are altered upon photodoping at both (π, π), and $(\pi, 0)$.

Further insight into the transient short-range correlations is gained from a quantitative analysis of the excitation spectra. A sum of four Gaussian-shaped peaks was used to represent the energy-loss data in Fig. 2 *A* and *B* (see dotted lines in the figure and *Materials and Methods* for further information). The fit shows that the magnon and orbital amplitudes are suppressed in the transient state and that their width is enlarged (see Fig. 3 *A* and *B*). Notably, at the magnetic wavevector the fitting parameters are most strongly modified at 0.5 ps and recover only partially within 5 ps, which is in line with the incomplete recovery of magnetic long-range order (see Fig. 1*B*).

Discussion

The cross-section of the orbital excitation around 680 meV is dependent on the respective charge occupations of the $J_{\text{eff}} = 3/2$ and $J_{\text{eff}} = 1/2$ state. The intensity would, for instance, decrease if fewer than four electrons per Ir side reside in the $J_{\text{eff}} = 3/2$ ground state and increase if the $J_{\text{eff}} = 1/2$ state was empty. The transient depletion of the excitation thus provides direct evidence that not only $J_{\text{eff}} = 1/2$ but also 3/2 electrons are pumped over the insulating band gap, and that some of

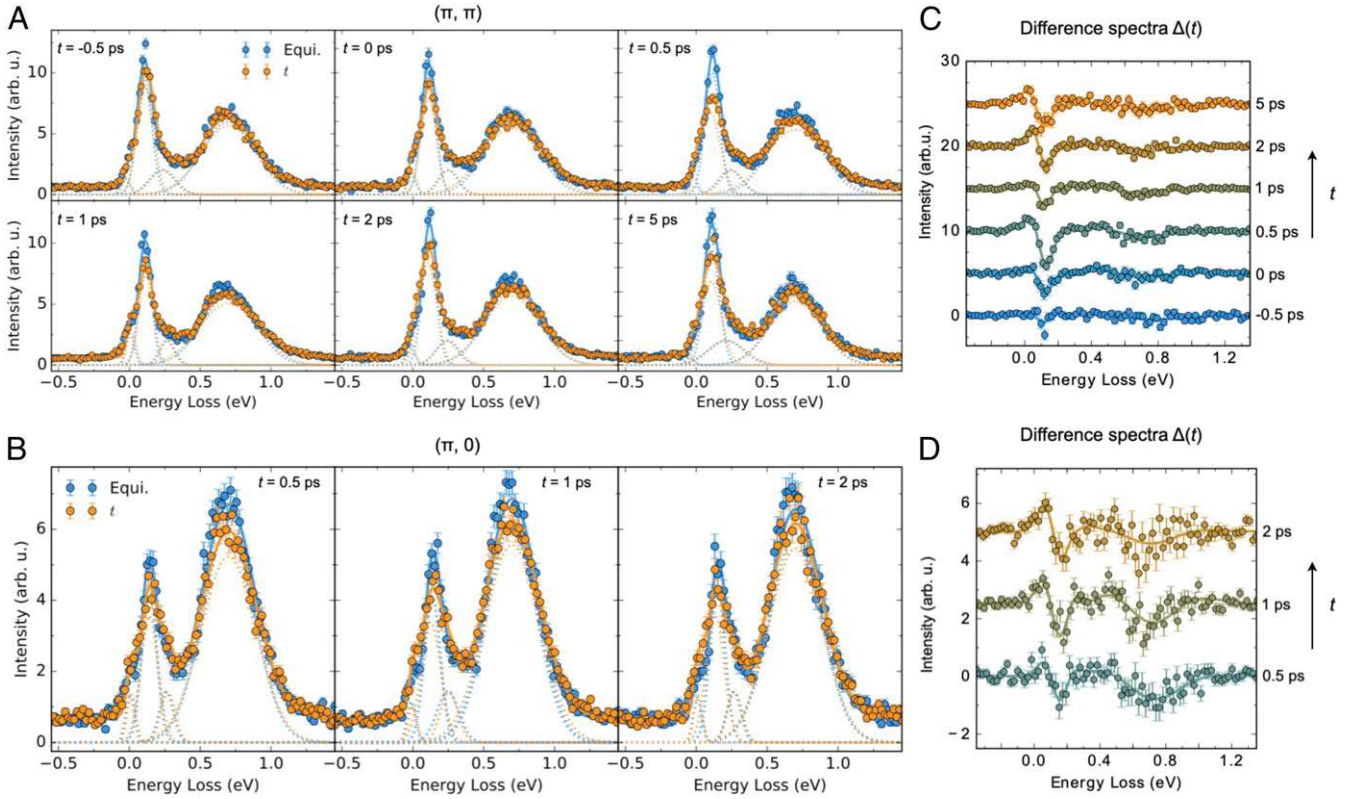

Fig. 2. Static and transient electronic short-range correlations of $Sr_3Ir_2O_7$. Tr-RIXS spectra at the minimum (*A*) and maximum (*B*) of the dispersion. The spectra show an elastic line, a magnon, a magnon continuum, and an orbital excitation at ∼680 meV, before the arrival of the laser pump (blue) and for different time delays (orange). Error bars are determined via Poissonian statistics. The dotted lines are contributions of best fits to the data (solid lines), consisting of four Gaussians and a constant background. Their difference spectra are shown in *C* and *D*.

the $J_{\text{eff}} = 3/2$ carriers do not decay into their orbital ground state within 5 ps. This supports a picture in which the electronic subsystem remains in a transient state for appreciable time delays.

Having established the dynamics of the orbital excitation, we now turn to the transient behavior of the collective (pseudo-)spins. In equilibrium, magnetic long-range order ensures the existence of well-defined spin-waves. Upon photoexcitation, broader peaks are observed while the magnetic exchange couplings are unaffected. This can be conceptualized as a redistribution of magnons out of the modes populated in equilibrium into a range of transient magnons around the original mode. Our data allow us to directly investigate how magnons are modified at different delays after photoexcitation and to examine how they change across the Brillouin zone using (π, π) and $(\pi, 0)$ as representative points.

The substantial anisotropy perpendicular to the tetragonal plane leads to collinear magnetic long-range order, revealing a large magnon gap that is minimal at (π, π) and maximal at $(\pi, 0)$ (cf. Fig. 4*B* for details) (20–24). Thus, the results in Fig. 3*A* show that magnons are modified over an extended area in reciprocal space and that these changes persist for several picoseconds. This experimental result is strikingly different from the behavior in materials hosting a gapless excitation spectrum. In isotropic Heisenberg-like Sr_2IrO_4 (see Fig. 4*A*), for instance, the only observable changes in the magnon occurred at the magnetic Brillouin zone center of (π, π) (2). In the following discussion, we aim to assess these differences.

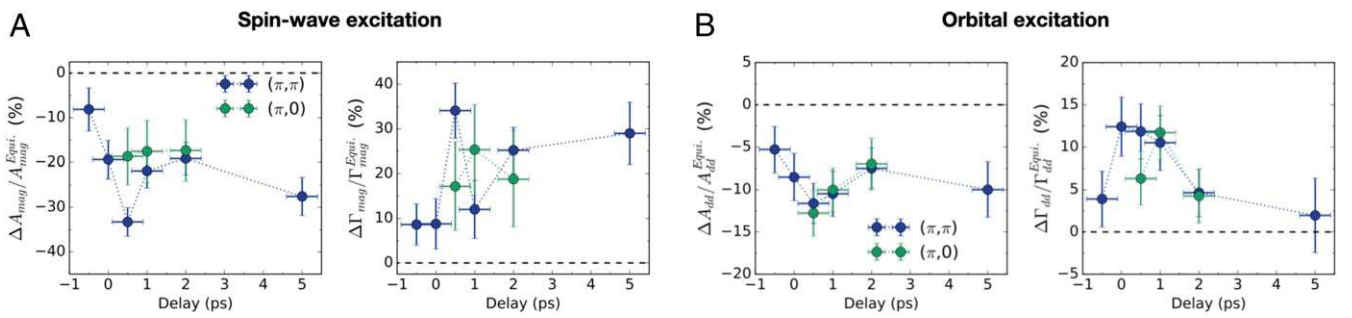

Fig. 3. Ultrafast evolution of electronic correlations in $Sr_3Ir_2O_7$. Time dependence of the relative (*A*) magnon and (*B*) orbital amplitude, *A*, and full width at half maximum (FWHM), Γ, respectively. The magnon and orbital amplitudes are suppressed in the transient state and their width is enlarged. Note the difference in scale. Error bars are derived from the least-squares fitting algorithm.

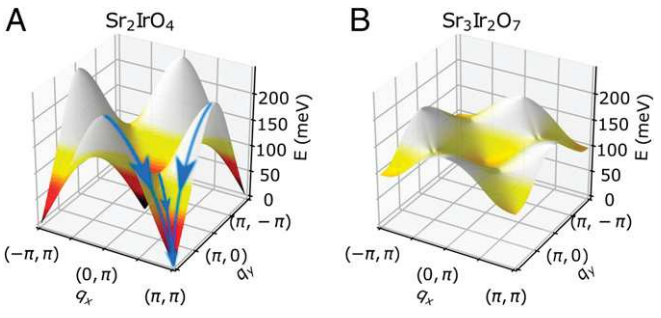

Fig. 4. Spin-bottleneck mechanism. (*A*) Heisenberg-like Sr_2IrO_4 features a near-zero-energy Goldstone mode establishing a well-defined channel (indicated schematically by the blue arrows) over which transient correlations decay into lower-energy multiparticle excitations. This leads to strong differences in the ultrafast magnetic response at (π, π) and $(\pi, 0)$. (*B*) Such a decay channel is absent in gapped antiferromagnet $Sr_3Ir_2O_7$, leading to transient magnons that are trapped in the entire Brillouin zone.

The transient state created here features suppressed magnetic long- and short-range correlations throughout the Brillouin zone and it, therefore, has some similarities to a thermal state at elevated temperature. This state, however, appears to form effectively instantaneously, within our time resolution of either 150 or 400 fs depending on whether one considers the REXS or RIXS signatures. These timescales are much faster than typical thermalization processes in magnetic insulators, ranging from several to hundreds of picoseconds (27–30). We thus consider the physical mechanisms at play, beyond a simple effective temperature model.

The photo-excitation process promoting charge carriers across the insulating gap leaves behind local spin vacancies that create nonthermal magnons spread across the entire Brillouin zone. These high-energy magnons can decay into lower-energy multiple-particle excitations via magnon–magnon scattering processes following the dispersion relation—which, in lowest approximation, is similar to the one of the unperturbed state. A full thermalization of the system, however, requires coupling to other subsystems, which becomes unavoidable for the dissipation of transient magnons around the minimum of the dispersion relation.

In gapless antiferromagnets, such as Sr_2IrO_4 (25, 31), a steep magnon dispersion from high to effectively zero energy establishes a well-defined decay channel (see Fig. 4*A*). Thus, spin waves at high energy face multiple possibilities to disintegrate, but the options become increasingly limited around the minimum of the Goldstone-like mode. This gives a natural explanation of why ultrafast magnons were observed only at (π, π) but not at $(\pi, 0)$ for Sr_2IrO_4 (2). Furthermore, the small spin-wave gap enables an efficient energy transfer into the lattice subsystem via low-energy phonons, restoring the equilibrium configuration.

We note that Néel order in Sr_2IrO_4 is unstable if one considers only a single Ir layer but stabilized by a very small interlayer c-axis coupling amplified by a divergence in the in-plane magnetic correlation length within the Ir layers (see *SI Appendix*). This is in strong contrast to bilayer materials such as $Sr_3Ir_2O_7$ which order magnetically without necessarily invoking coupling between different bilayers. Although the bilayer system features far stronger anisotropy and intrabilayer coupling, this is offset by the spin gap impeding the growth of the in-plane magnetic correlation proceeding the transition. Empirically, $Sr_3Ir_2O_7$ and Sr_2IrO_4 feature comparable Néel temperatures (285 and 240 K, respectively) despite the spin-wave gap of the former material being roughly 150 times larger (see Fig. 4) (20, 25, 31). Thus, no pronounced decay channel is present in $Sr_3Ir_2O_7$, which inherently limits the thermalization of transient magnons along a particular wavevector. Furthermore, phonon-assisted energy transfer processes are strongly reduced by the large spin gap, leading to long-lived magnons that are trapped over a large reciprocal space area.

Following this argument, the partial recovery of magnetic long-range order at a picosecond timescale may arise from two mechanisms. The magnetic time constant is close to the charge timescale that has been reported previously via ultrafast reflectivity measurements (32). This may attest to a link between charge and magnetic degrees of freedom, which is also supported by the wavevector-independent suppression of the orbital excitation below 2 ps (see Fig. 3*B*). In Mott materials the (pseudo-)spin configuration is directly related to the charge distribution on the atomic sites, whose recovery reinstates the original one spin/site population. Thus, it is conceivable to attribute the partial recovery of magnetic order in $Sr_3Ir_2O_7$ to its Mott nature. Alternatively, the partial recovery of magnetic long-range order may originate from a redistribution of transient magnons within the Brillouin zone, pointing toward a scenario in which the laser pump generates an excess of magnons at the magnetic wavevector. In fact, the results shown in Fig. 3*A* suggest a suppression of spin waves at (π, π), which is absent at $(\pi, 0)$.

In summary, we report a near-instantaneous creation of transient magnons in the gapped antiferromagnet $Sr_3Ir_2O_7$ after a laser excitation of 2 μm. The ultrafast transverse short-range correlations occur at both extremes of the magnetic dispersion in momentum space, showing the existence of trapped spin waves that are likely present throughout the entire Brillouin zone. This demonstrates an incoherent response of transient magnetism, which is fundamentally different from in gapless antiferromagnets such as in Heisenberg-like Sr_2IrO_4 (2). The results are interpreted in the context of a spin-bottleneck effect. In Sr_2IrO_4 a steep dispersion exists from high energy magnons at the magnetic zone boundary into low-energy magnons at (π, π), which allows for a highly efficient magnon decay. In contrast, the large magnon gap and moderate dispersion of $Sr_3Ir_2O_7$ leads to transient spin waves that are trapped in the entire Brillouin zone. Thus, our results emphasize the need to include contributions like anisotropic magnetic exchange interactions alongside electron–phonon couplings in theoretical approaches that model transient magnetic states. Finally, we remind the reader that neither a collinear antiferromagnetic spin alignment nor magnons are exact eigenstates of an $S = 1/2$ quantum magnet. Thus, it may be natural to expect strong magnon–magnon scattering occurs in some transient states. Further experimental and theoretical efforts along these lines will be vital to progress in the understanding of the ultrafast dynamics in quantum materials, including cases where complex competitions of macroscopic quantum phases appear via photodoping.

Materials and Methods

Sample Preparation and Characterization.

All measurements were performed on $Sr_3Ir_2O_7$ single crystals that were grown with a flux method as described in ref. 33 and references therein. The high quality of the crystals was confirmed via Laue and single-crystal diffraction. Here, we denote reciprocal space using a pseudo-tetragonal unit cell with a = 3.896 Å and c = 20.88 Å at room temperature.

All experiments were conducted on the same sample with crystal orientations [1, 0, 0] and [0, 0, 1] or [1, 1, 0] and [0, 0, 1] in the scattering plane for tr-REXS or tr-RIXS experiments, respectively. In both cases, a horizontal scattering geometry was used and the sample was cooled to $T \approx 110$ K via nitrogen cryostreams.

Optical Laser Pump.

One hundred-femtosecond-long pump pulses of 620 meV (2 μm) were generated by an optical parametric amplifier similar to previous ultrafast experiments on Sr_2IrO_4 (2). The angle between the

incident X-ray and infrared pulses was 20°. This leads to an estimated laser penetration depth of ∼82 nm for grazing incident X-rays (see *SI Appendix*).

tr-REXS.

The ultrafast recovery of magnetic long-range order was studied at beamline 3 of the SPring-8 Angstrom Compact free-electron LAser (SACLA) featuring a repetition rate of 30 Hz (34, 35). The X-ray energy was tuned to the Ir L_3-edge at 11.215 keV and refined via a resonant energy scan of the (−3.5, 1.5, 18) magnetic Bragg peak. The reflection was detected at $2\theta = 92.2°$ using a multiport charged coupled device area detector (0.0086 r.l.u. per pixel) (36). The Bragg condition was established by rotating the sample surface normal $\Delta\chi = 21.2°$ out of the scattering plane. The X-rays were focused to a spot size of 20-μm FWHM and hit the sample at a grazing angle of ∼ 1.6°. The X-ray penetration depth was estimated to 162 nm (see *SI Appendix*). The laser spot size was ∼230-μm FWHM at normal incidence. The detector was read out shot-by-shot and thresholded to reduce background arising from X-ray fluoresence and electrical noise. Two-dimensional detector images were integrated around the position where the Bragg peak was observed. Each data point contains statistics from 300 to 600 shots. The 300-fs jitter of the free electron laser was corrected with a GaAs timing tool for delays $t < 7$ ps, yielding an effective time resolution of 150 fs at FWHM (37).

Fig. 1*B* reports the magnetic Bragg peak ratio I_{on}/I_{off}, where I_{on} denotes the intensity after laser excitation and I_{off} when the laser was switched off. It is noted that even for strong fluences some remnant magnetic signal is observed for $t > 0$, suggesting some experimental mismatch between pumped laser and probed X-ray volumes Further information on the time evolution of the magnetic order parameter is given in *SI Appendix*.

tr-RIXS.

The ultrafast recovery of magnetic short-range correlations was studied at the X-ray Pump Probe instrument of the Linac Coherent Light Source (LCLS) running at a repetition rate of 120 Hz (38). The data at (π, π) and $(\pi, 0)$ correspond to measurements at (−3.5, 0.5, 20) and (−3.5, 0, 19.6) with $2\theta = 93.7$ and 91.8°. The X-rays were focused to a spot size of 50-μm FWHM. We used a grazing incident geometry of 3.7 and 2.1° for the two reciprocal lattice positions, yielding an X-ray penetration depth of 378 and 214 nm, respectively (see *SI Appendix*). The laser spot size equaled 845-μm FWHM at normal incidence and the fluence was fixed to 20 mJ/cm^2. The same RIXS spectrometer as in ref. 2 was used, delivering an energy resolution of ∼ 70 meV with an angular acceptance of 6° (0.28 Å^{-1}) on the analyzer. The ePix100a area detector was read out every shot (39). The time resolution of the experiment arising from a combined jitter and beam drift effect was limited to ∼0.4 ps. It is noted that it proved impractical to use the timing tool, as it was insufficiently sensitive on the aggressively monochromatized incident beam. RIXS spectra were collected in a stationary mode of 144,000 shots each. Two to six acquisitions were taken for each time delay. The data presented in Fig. 2 *A* and *B* were normalized to an incident beam intensity monitor and calibrated to the energy of the orbital excitation at 680 meV (20–23). The center of the elastic line and its width were fixed in the analysis to 0 meV and the experimental resolution, respectively. Robust fits were obtained by further constraining the energy of the magnon continuum to 260 meV and its amplitude to the mean values of 2.02 and 1.44 for (π, π) and $(\pi, 0)$, respectively. All other parameters were varied freely and are shown in *SI Appendix*, Fig. S2.

Data Availability. All study data are included in the article and/or *SI Appendix*.

ACKNOWLEDGMENTS. We thank Chris Homes for discussions. The design, execution of the experiments, and the data analysis are supported by the US Department of Energy (DOE), Office of Science, Basic Energy Sciences, Materials Science and Engineering Division, under Contracts DE-SC0012704(BNL) and DE-AC02-06CH11357(ANL). D.G.M. acknowledges funding from the Swiss National Science Foundation, Fellowship P2EZP2_175092. C.D.D. was supported by the Engineering and Physical Sciences Research Council (EPSRC) Centre for Doctoral Training in the Advanced Characterization of Materials under Grant EP/L015277/1. X.L. and J. Lin were supported by the ShanghaiTech University startup fund MOST of China under Grant 2016YFA0401000, National Natural Science Foundation of China under Grant 11934017, and the Chinese Academy of Sciences under Grant 112111KYSB20170059. Work at University College London was supported by the EPSRC under Grants EP/N027671/1 and EP/N034872/1. The work at the Institute of Photonic Sciences received financial support from the Spanish Ministry of Economy and Competitiveness through the "Severo Ochoa" program for Centers of Excellence in R&D (SEV-2015-0522), from Fundació Privada Cellex, from Fundació Mir-Puig, and from Generalitat de Catalunya through the CERCA program and from the European Research Council under the European Union's Horizon 2020 research and innovation program (Grant Agreement 758461). J. Liu. acknowledges support from the NSF under Grant DMR-1848269. The magnetic Bragg peak measurements were performed at BL3 of SACLA with the approval of the Japan Synchrotron Radiation Research Institute (Proposals 2017A8077, 2018A8032, and 2019A8087). This research made use of the LCLS, SLAC National Accelerator Laboratory, which is a DOE Office of Science User Facility, under Contract DE-AC02-76SF00515.

1. R. D. Averitt, A. J. Taylor, Ultrafast optical and far-infrared quasiparticle dynamics in correlated electron materials. *J. Phys. Condens. Matter* **14**, R1357–R1390 (2002).
2. M. P. M. Dean *et al.*, Ultrafast energy- and momentum-resolved dynamics of magnetic correlations in the photo-doped mott insulator Sr_2IrO_4. *Nat. Mater.* **15**, 601–605 (2016).
3. D. N. Basov, R. D. Averitt, D. Hsieh, Towards properties on demand in quantum materials. *Nat. Mater.* **16**, 1077 (2017).
4. M. Gandolfi, G. L. Celardo, F. Borgonovi, G. Ferrini, A. Avella, F. Banfi, C. Giannetti, Emergent ultrafast phenomena in correlated oxides and heterostructures. *Phys. Scripta* **92**, 034004 (2017).
5. Y. Wang *et al.*, Theoretical understanding of photon spectroscopies in correlated materials in and out of equilibrium. *Nat. Rev. Mater.* **3**, 312–323 (2018).
6. Y. Cao *et al.*, Ultrafast dynamics of spin and orbital correlations in quantum materials: An energy- and momentum-resolved perspective. *Phil. Trans. Math. Phys. Eng. Sci.* **377**, 20170480 (2019).
7. S. Wall *et al.*, Ultrafast disordering of vanadium dimers in photoexcited VO_2. *Science* **362**, 572–576 (2018).
8. D. Fausti *et al.*, Light-induced superconductivity in a stripe-ordered cuprate. *Science* **331**, 189–191 (2011).
9. C. Tzschaschel, T. Satoh, M. Fiebig, Tracking the ultrafast motion of an antiferromagnetic order parameter. *Nat. Commun.* **10**, 3995 (2019).
10. A. Simoncig *et al.*, Generation of coherent magnons in NiO_2 stimulated by EUV pulses from a seeded free-electron laser. *Phys. Rev. Materials* **1**, 073802 (2017).
11. B. Keimer, J. E. Moore, The physics of quantum materials. *Nat. Phys.* **13**, 1045 (2017).
12. G. Coslovich *et al.*, Ultrafast charge localization in a stripe-phase nickelate. *Nat. Commun.* **4**, 2643 (2013).
13. L. Savary, L. Balents, Quantum spin liquids: A review. *Rep. Prog. Phys.* **80**, 016502 (2016).
14. A. Secchi, S. Brener, A. I. Lichtenstein, M. I. Katsnelson, Non-equilibrium magnetic interactions in strongly correlated systems. *Ann. Phys.* **333**, 221 (2013).
15. N. Bittner, D. Golež, H. U. R. Strand, M. Eckstein, P. Werner, Coupled charge and spin dynamics in a photo-excited Mott insulator. *Phys. Rev. B* **97**, 235125 (2018).
16. J. H. Mentink, Manipulating magnetism by ultrafast control of the exchange interaction. *J. Phys. Condens. Matter* **23**, 453001 (2017).
17. J. H. Mentink, K. Balzer, M. Echkstein, Ultrafast and reversible control of the exchange interaction in Mott insulators. *Nat. Commun.* **6**, 6708 (2015).
18. S. J. Moon *et al.*, Dimensionality-controlled insulator-metal transition and correlated metallic state in 5*d* transition metal oxides $Sr_{n+1}Ir_nO_{3n+1}$: ($n = 1$, 2, and ∞). *Phys. Rev. Lett.* **101**, 226402 (2008).
19. D. Afanasiev *et al.*, Ultrafast spin dynamics in photodoped spin-orbit Mott insulator Sr_2IrO_4. *Phys. Rev. X* **9**, 021020 (2019).
20. J. Kim *et al.*, Large spin-wave energy gap in the bilayer iridate $Sr_3Ir_2O_7$: Evidence for enhanced dipolar interactions near the Mott metal-insulator transition. *Phys. Rev. Lett.* **109**, 157402 (2012).
21. M. Moretti Sala *et al.*, Evidence of quantum dimer excitations in $Sr_3Ir_2O_7$. *Phys. Rev. B* **92**, 024405 (2015).
22. X. Lu *et al.*, Doping evolution of magnetic order and magnetic excitations in $(Sr_{1-x}La_x)_3Ir_2O_7$. *Phys. Rev. Lett.* **118**, 027202 (2017).
23. X. Lu *et al.*, Dispersive magnetic and electronic excitations in iridate perovskites probed by oxygen *K*-edge resonant inelastic x-ray scattering. *Phys. Rev. B* **97**, 041102 (2018).
24. G. Cao, P. Schlottmann, The challenge of spin–orbit-tuned ground states in iridates: A key issues review. *Rep. Prog. Phys.* **81**, 042502 (2018).
25. J. Kim *et al.*, Magnetic excitation spectra of Sr_2IrO_4: Probed by resonant inelastic x-ray scattering: Establishing links to cuprate superconductors. *Phys. Rev. Lett.* **108**, 177003 (2012).
26. B. J. Kim *et al.*, Phase-sensitive observation of a spin-orbital Mott state in Sr_2IrO_4. *Science* **323**, 1329–1332 (2009).
27. A. V. Kimel, R. V. Pisarev, J. Hohlfeld, Th. Rasing, Ultrafast quenching of the antiferromagnetic order in $FeBo_3$: Direct optical probing of the phonon-magnon coupling. *Phys. Rev. Lett.* **89**, 287401 (2002).
28. A. V. Kimel *et al.*, Optical excitation of antiferromagnetic resonance in $TmFe_3$. *Phys. Rev. B* **74**, 060403 (2006).
29. M. Matsubara, Y. Okimoto, T. Ogasawara, Y. Tomioka, H. Okamoto, Y. Tokura, Ultrafast photoinduced insulator-ferromagnet transition in the perovskite manganite $Gd_{0.55}Sr_{0.45}MnO_3$. *Phys. Rev. Lett.* **99**, 207401 (2007).

30. H. Yada *et al.*, Discrimination between photodoping- and heat-induced magnetization changes in $Nd_{0.52}Sr_{0.48}MnO_3$ using a heterostructure with $SrTiO_3$. *Phys. Rev. B* **84**, 045114 (2011).
31. S. Calder, D. M. Pajerowski, M. B. Stone, A. F. May, Spin-gap and two-dimensional magnetic excitations in Sr_2IrO_4. *Phys. Rev. B* **98**, 220402 (2018).
32. H. Chu *et al.*, A charge density wave-like instability in a doped spin–orbit-assisted weak Mott insulator. *Nat. Mater.* **16**, 200 (2017).
33. L. Li *et al.*, Tuning the $J_{\text{eff}} = \frac{1}{2}$ insulating state via electron doping and pressure in the double-layered iridate $Sr_3Ir_2O_7$. *Phys. Rev. B* **87**, 235127 (2013).
34. Z. Huang, I. Lindau, Sacla hard-x-ray compact fel. *Nat. Photonics* **6** (8), 505–506 (2012).
35. K. Tono *et al.*, Beamline, experimental stations and photon beam diagnostics for the hard X-ray free electron laser of SACLA. *New J. Phys.* **15**, 083035 (2013).
36. T. Kameshima *et al.*, Development of an X-ray pixel detector with multi-port charge-coupled device for X-ray free-electron laser experiments. *Rev. Sci. Instrum.* **85**, 033110 (2014).
37. T. Katayama *et al.*, A beam branching method for timing and spectral characterization of hard X-ray free-electron lasers. *Struct. Dynam.* **3**, 034301 (2016).
38. M. Chollet *et al.*, The X-ray pump-probe instrument at the Linac Coherent Light Source. *J. Synchrotron Radiat.* **22**, 503–507 (2015).
39. G. A. Carini *et al.*, Epix100 camera: Use and applications at LCLS. *AIP Conf. Proc.* **1741**, 040008 (2016).